








RESEARCH ARTICLE | JULY 05 2023

Estimating the neutron yield in a deuterium plasma with the JET neutron camera

Linus Hägg ; Federico Binda ; Sean Conroy; Göran Ericsson ; Zamir Ghani; Luca Giacomelli ; Daniele Marocco ; Alberto Milocco; Marco Riva ; Erik Andersson Sundén ; JET Contributors



Rev. Sci. Instrum. 94, 073502 (2023)

<https://doi.org/10.1063/5.0144654>



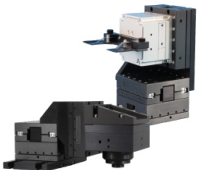
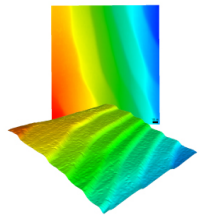
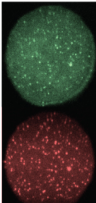


View
Online



Export
Citation

CrossMark

 <p>MCL MAD CITY LABS INC. www.madcitylabs.com</p>	<p>Nanopositioning Systems</p> 	<p>Modular Motion Control</p> 	<p>AFM and NSOM Instruments</p> 	<p>Single Molecule Microscopes</p> 
--	--	--	---	--

Estimating the neutron yield in a deuterium plasma with the JET neutron camera

Cite as: *Rev. Sci. Instrum.* **94**, 073502 (2023); doi: [10.1063/5.0144654](https://doi.org/10.1063/5.0144654)

Submitted: 31 January 2023 • Accepted: 5 June 2023 •

Published Online: 5 July 2023



View Online



Export Citation



CrossMark

Linus Hägg,^{1,a)} Federico Binda,^{2,b)} Sean Conroy,¹ Göran Ericsson,¹ Zamir Ghani,³ Luca Giacomelli,⁴ Daniele Marocco,⁵ Alberto Milocco,⁶ Marco Riva,⁵ Erik Andersson Sundén,¹ and JET Contributors^{c)}

AFFILIATIONS

¹Department of Physics and Astronomy, Uppsala University, SE-751 05 Uppsala, Sweden

²Översättravägen 17, 184 70 Åkersberga, Stockholms län, Sweden

³United Kingdom Atomic Energy Authority, Culham Science Centre, Abingdon, Oxon OX14 3DB, United Kingdom

⁴European Commission—Joint Research Centre, Via Enrico Fermi 2749, 21027 Ispra, VA, Italy

⁵Fusion and Technology for Nuclear Safety and Security Department, ENEA, C.R. Frascati, Via E. Fermi 45, I-00044 Frascati, Roma, Italy

⁶University of Milano–Bicocca University, Physics Department “G. Occhialini,” Milano, Italy

^{a)} Author to whom correspondence should be addressed: linus.hagg@physics.uu.se

^{b)} Previously affiliation: Uppsala University.

^{c)} See the author list of “Overview of JET results for optimising ITER operation” by J. Mailloux *et al.*, *Nucl. Fusion* **62**, 042026 (2022).

ABSTRACT

The JET neutron camera is a well-established detector system at JET, which has 19 sightlines each equipped with a liquid scintillator. The system measures a 2D profile of the neutron emission from the plasma. A first principle physics method is used to estimate the DD neutron yield that is based on JET neutron camera measurements and is independent of other neutron measurements. This paper details the data reduction techniques, models of the neutron camera, simulations of neutron transport, and detector responses used to this end. The estimate uses a simple parameterized model of the neutron emission profile. The method makes use of the JET neutron camera’s upgraded data acquisition system. It also accounts for neutron scattering near the detectors and transmission through the collimator. These components together contribute to 9% of the detected neutron rate above a 0.5 MeV energy threshold. Despite the simplicity of the neutron emission profile model, the DD neutron yield estimate falls on average within 10% agreement with a corresponding estimate from the JET fission chambers. The method can be improved by considering more advanced neutron emission profiles. It can also be expanded to estimate the DT neutron yield with the same methodology.

© 2023 Author(s). All article content, except where otherwise noted, is licensed under a Creative Commons Attribution (CC BY) license (<http://creativecommons.org/licenses/by/4.0/>). <https://doi.org/10.1063/5.0144654>

I. INTRODUCTION

Neutrons are a valuable source of information in the study of tokamak fusion plasmas. Not only does the neutron rate relate to the fusion reaction rate, which in turn relates to fusion power, but neutron measurements can be used to estimate a host of other plasma parameters. In this paper, we concern ourselves with fusion reactions between plasma ions that generate neutrons, mainly DD reactions where two deuterons react. If tritium is present deuterons and tritons can react (DT) and also produce neutrons. If the deuterons in the plasma have a low temperature, the neutrons resulting from

DD reactions (henceforth referred to as “DD neutrons”) will have an average energy of 2.45 MeV. In a fusion plasma, the energy distribution of the neutrons is dependent on the velocity distribution of the reactants.^{1–4} Neutron measurements can therefore be used to investigate the ion velocity distribution of the plasma ions,^{5–7} which in turn helps in estimating other plasma parameters such as the ion temperature,^{8,9} the ion densities,^{10–13} the plasma rotation,¹⁴ and the fraction of neutrons emitted in reactions between thermal ions to those emitted in reactions involving non-thermal fuel ions.^{15,16} However, relating neutron measurements to these physics quantities requires modeling of the neutron spectra in the plasma,

the neutron transport to the detector, and the subsequent detector response.

This paper describes a method for estimating the DD neutron yield using neutron emission profile models and measurement data from the JET neutron profile monitor,^{17,18} also known as the neutron camera. The method is compared to another independent estimate of the DD neutron yield from the JET fission chambers.¹⁹ The JET neutron camera has been used for similar works in the past. In 1994, a model of the neutron camera was used for the purpose of a DD and DT absolute calibration.²⁰ In 1995, the neutron camera geometry was upgraded. In 2004, DT measurement data from the neutron camera were used to estimate the neutron yield from the plasma in trace tritium experiments.²¹ The camera's data acquisition system was upgraded in 2009 (the so-called KN3N) where the analog-to-digital converters (ADC) were replaced with digital cards.²² With this upgrade, the energy information for each recorded event can be stored and utilized. Among other things, it allows for flexibility in the setting of pulse height (energy) thresholds and a more accurate event identification, both of which are utilized in this work. In 2010, the neutron camera was used to estimate the total JET neutron yields together with the MPR spectrometer,²³ though that work was still using the old data acquisition system. A first attempt to exploit the new data acquisition system for neutron emission spectroscopy analysis (NES) was reported in Ref. 24, and the possibility to recover information on the ion temperature profile and on the relative contributions of thermal and non-thermal components to the neutron emission was shown. As stated by the authors, results were affected by large uncertainties since the detectors of the camera lacks of photomultiplier stability monitors and the analysis was performed without any attempt to correct the raw data for background and using a single set of simulated response functions for all detectors. This work improves upon previous attempts to utilize the neutron camera to estimate the DD neutron yield.

This paper is organized as follows: Sec. II describes the JET neutron camera and the different models of the camera that were used. Section III shows how the camera data are processed into pulse height spectra and how the detectors are calibrated. Section IV details the neutron emission profile models and the simulations of neutron production, neutron transport, detector response to different neutron energies, tokamak far-wall backscatter, and in-scatter in structures close to the detectors. In Sec. V, the modeled neutron emission profile is fitted to measurement data and the DD neutron yield is estimated. In the end, Sec. VI covers discussion and conclusions.

II. THE NEUTRON CAMERA

The JET neutron camera provides measurements that can be used to obtain the neutron emission profile at JET. It has 19 lines of sight equipped with NE213 liquid scintillators²⁵ for detecting DD neutrons and BC418 plastic scintillators²⁶ dedicated to measuring DT neutrons. An illustration of the camera's 19 sightlines is shown in Fig. 1.

Neutrons reaching the neutron profile monitor are categorized according to their origin. In this work, we consider three neutron components; direct, in-scatter, and backscatter. The direct component consists of neutrons that reach the detectors unhindered, i.e., without undergoing any scattering on its way from production to detection. The in-scatter component includes those that scatter from material near the detectors. The backscatter component describes neutrons that scatter against the torus back wall.²⁸

To simulate the three components, three different models of the neutron camera are used in this paper. The first two are MCNP (Monte Carlo N-Particle) models, and the last is an optical model. For the purpose of simulating backscatter neutrons, an MCNP model is used that includes the JET torus wall and much of the material surrounding the neutron camera, as seen in Fig. 1(a). From

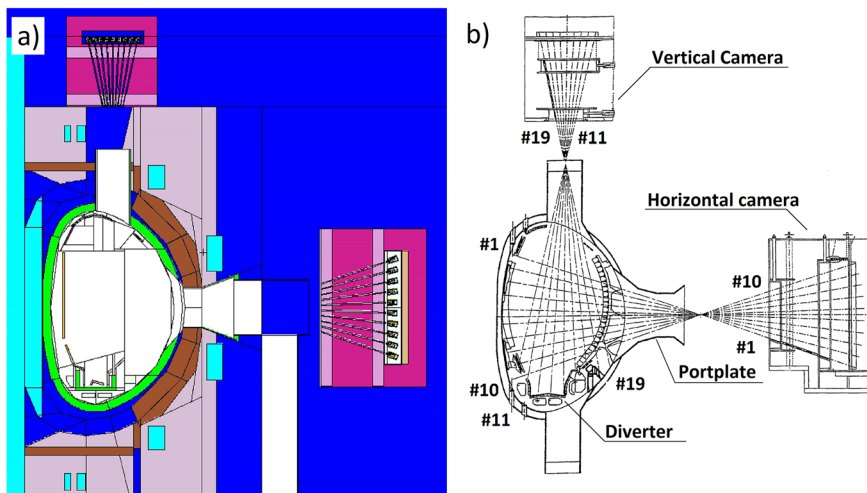


FIG. 1. The JET neutron camera and its 19 sightlines through a slice of the JET torus. (a) is a poloidal cross-section of the MCNP JET model. (b) is adapted from JG96.200-3c in the JET Figure Database.²⁷

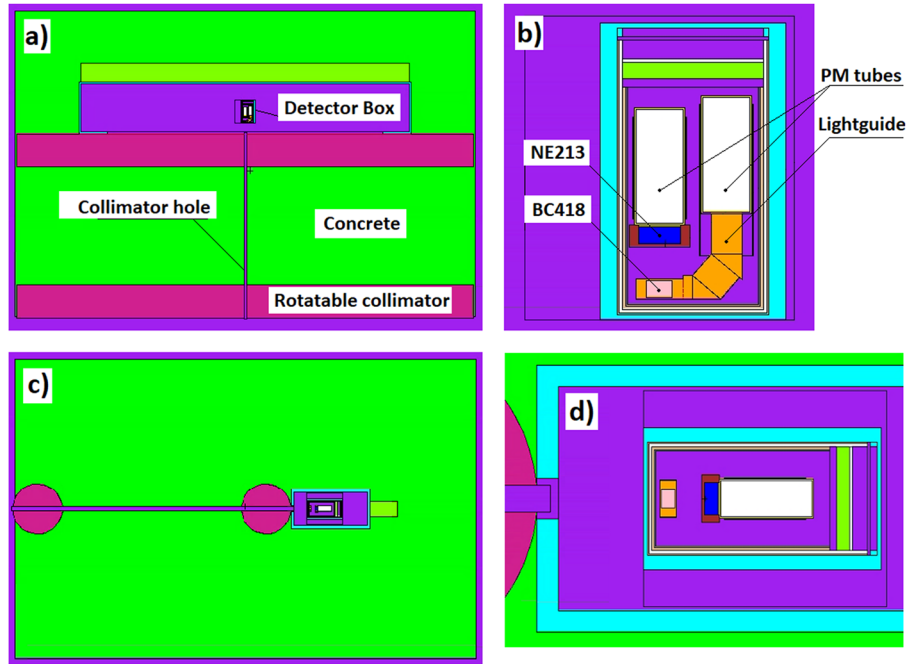


FIG. 2. The MCNP detector system model. (a) shows a cross section of the channel 5 detector box, the surrounding concrete in green, and the rotatable detector cylinders in red. (b) shows a close-up of the detector box, which contains the NE213 scintillator, the BC418 scintillator, lightguides, their respective photomultiplier tubes, and the surrounding structural and shielding material. The detector box is based on JG95.166-1c in the JET Figure Database²⁷. (c) and (d) show the same components but with a perpendicular cross section relative to (a) and (b).

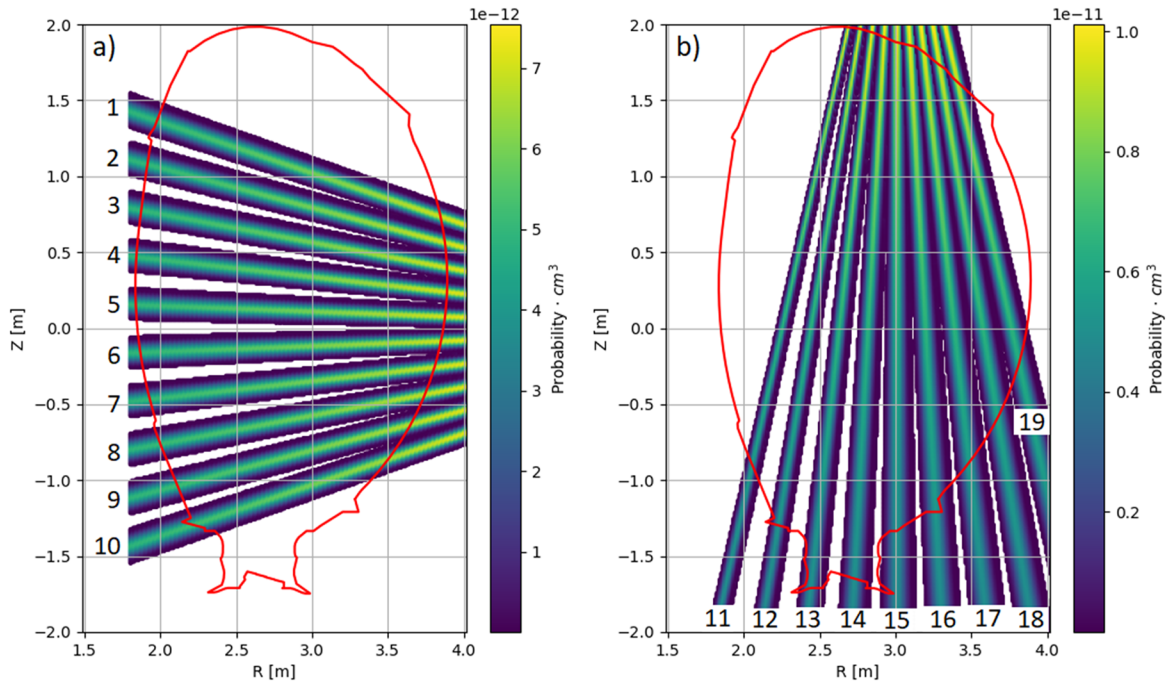


FIG. 3. The LINE2.1 visibility cones in relation to the first wall. The intensity of a point in a channel's visibility cone indicates how visible the detector is from that point. Shown for the horizontal (a) and vertical (b) camera channels.

here on, we refer to this model as the JET model. Similar variants of the JET model have been used to great effect in Refs. 28 and 29. The second MCNP model is used to calculate the in-scatter component. This model is more detailed than the JET model but only contains the channel 5 collimator, the detector box, and the materials in its immediate surroundings. We refer to this as the detector system model. A cross section of the detector system model is seen in Fig. 2.

The optical model is called LINE2.1, in which the collimator and all other materials are considered to be perfect absorbers. LINE2.1 produces a voxel map over the tokamak volume. For each voxel, LINE2.1 calculates the probability of a neutron, drawn from an isotropic distribution, to reach the detector in each channel. The poloidal projection of the probability scaled with the respective voxel volume is shown in Fig. 3 together with the first wall of JET.

The collimator geometry in the neutron camera varies between channels in both length and aperture diameter. Because the detector system model is only based on one channel, it might appear to be overly simplified. However, as detailed in Sec. IV, the detector system model is used in conjunction with the LINE2.1 model, which contains the specific geometries for all channels. In this way, the method accounts for the more impactful geometrical differences, such as collimator diameter and length.

III. DATA PROCESSING AND DETECTOR CALIBRATION

The NE213 scintillator detectors are sensitive to both neutrons and gammas, which interact with protons and electrons, respectively. The slowing down of these secondary particles result in light production in the scintillator. The intensity of this light is related to the deposited energy of the secondary particle. A photo-multiplier tube attached to the scintillator³⁰ produces a voltage pulse and the integral of such a pulse gives a total charge value as a measure of the scintillator light yield. For electrons, the light yield per deposited energy is well approximated by a linear function, while for protons the relationship is non-linear.³⁰

Furthermore, due to the different physics behind the energy deposition of the neutron and gamma events, the resulting voltage pulses in the NE213 will have different shapes. As seen in Fig. 4, the voltage pulse from a gamma-induced event decays quickly from the initial peak. In contrast, a neutron-induced event decays more slowly so the voltage pulse will get a distinctly longer tail than the gamma event. This is utilized to classify events.

A. Data processing

Each individual voltage pulse is stored as a time series of voltage values in a record by the data acquisition system. Pulses are identified as either neutron or gamma events using a pulse shape discrimination (PSD) method. We designate two intervals, gates, over the voltage pulses. The short gate only spans the initial peak while the long gate extends over the decay tail, as seen in Fig. 4. Integrating the voltage values inside these gates for each event yields the corresponding short charges (Q_S) and long charges (Q_L). The ratio between them, $\frac{Q_S}{Q_L}$, is designated as the PSD factor, which is then compared to the integral Q_{tot} over the whole voltage pulse. The Q_{tot} value is proportional to the total charge of the pulse. The gates for a

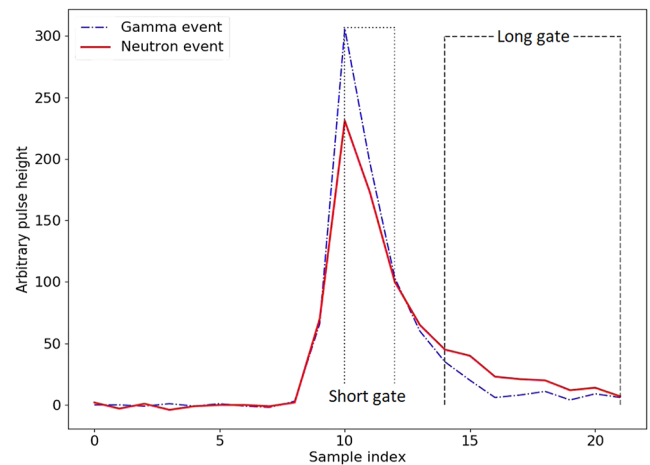


FIG. 4. Time sampled records of two voltage pulses from a gamma and a neutron event with equivalent Q_{tot} values. The boundaries of the short and long gates are shown as vertical lines. Data sourced from JET shot 86 825 channel 15.

neutron and a gamma event are exemplified in Fig. 4, where we also see the pulse shape difference.

The small tail of voltage pulses from gamma events earns them lower Q_L values compared to neutron events with equivalent Q_{tot} values. They subsequently earn higher PSD factors than neutron events. With carefully chosen gates the neutron and gamma events will be well separated, and this PSD separation can be seen in Fig. 5. Gamma events are located in the upper cluster, while neutron events end up in the lower cluster. Events that are further below the neutron cluster are recognized as pile-up events and random noise. A pile-up event occurs when two or more voltage pulses arrive close enough in time to overlap in the same record.

A selection of events is made by drawing a closed shape surrounding the neutron cluster in the PSD diagram and excluding events that fall outside the lines, as depicted in Fig. 5. This cluster is dominated by the neutron emission from the DD reactions. We refer to the closed shape as the PSD selection. This is done to exclude gamma events, noise, pile-up events, and some of the higher energy neutron events originating from DT reactions. At low energies (corresponding to low Q_{tot} values), the neutron and gamma events partially overlap, as a consequence some gamma events will fall inside the PSD selection. In order to make sure only neutrons are selected, an energy threshold is employed to only consider the well separated region at higher Q_{tot} values.

The Q_{tot} values of all selected events allows us to construct a pulse height spectrum (PHS) (see Fig. 6). Converting the Q_{tot} values into light yield requires a light yield calibration, and this is described in Sec. III B.

B. Calibration

Each detector is equipped with a ^{22}Na gamma source used for light yield calibration. The sources provide monoenergetic gammas at 0.511 and 1.275 MeV. Collected gamma events are identified with the PSD method, and their Q_{tot} values are used to construct a PHS. The measurement data can be fitted to a simulated gamma PHS

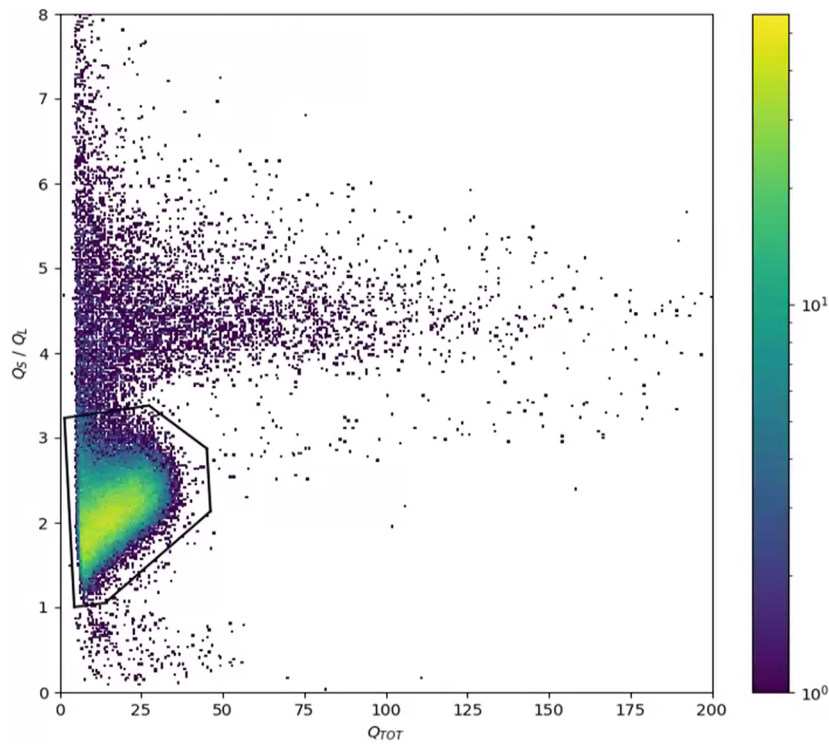


FIG. 5. PSD diagram of JET shot 96 095 for the neutron camera detector channel 15 in the time interval 49.5–49.9 s. The dark line surrounding the neutron cluster is the PSD selection.

based on Eqs. (1) and (2). The Q_{tot} value of each measured event is converted to light yield (MeVee) using

$$L [\text{MeVee}] = k \cdot Q[C] + m, \quad (1)$$

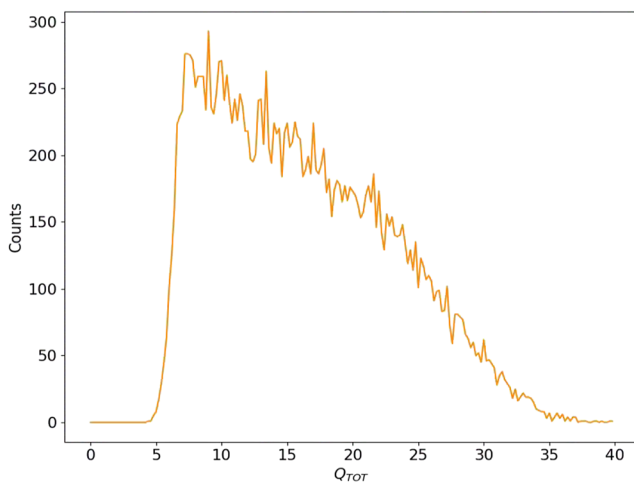


FIG. 6. Pulse height spectrum of the selected neutron events in Fig. 5. A hardware threshold excludes pulses with Q_{tot} values lower than 5 to remove noise.

where L is the light yield, Q is the total charge, and k and m are calibration parameters. The unit eVee stands for to electron equivalent energy, referring to light produced in the scintillator by an electron of that energy. Note that for electrons and gammas the produced light is linearly proportional to the deposited energy. The simulation accounts for the detector resolution with a Gaussian broadening given by

$$FWHM = a + b\sqrt{L + cL^2}, \quad (2)$$

where the resolution parameters a , b , and c describe the full width half maximum for a specific light yield L .³¹ The parameter c is more relevant for energies higher than 1.275 MeV.

The calibration is obtained as follows: The light yield response from a ^{22}Na gamma source in the detector box is first simulated in the detector system model without any Gaussian broadening included. The broadening is applied to the simulated PHS afterward such that the broadening coefficients can be adjusted. The parameters k , m , a , b , and c in Eqs. (1) and (2) are varied to fit the simulated and measured PHS to each other. This fit is done by minimizing CSTAT,³² a test statistic similar to χ^2 . CSTAT is defined as

$$CSTAT = 2 \sum_i (e_i - n_i \ln e_i), \quad (3)$$

where n_i are binned measurement values and e_i are binned fitted values. For CSTAT the fluctuation of the data is assumed to

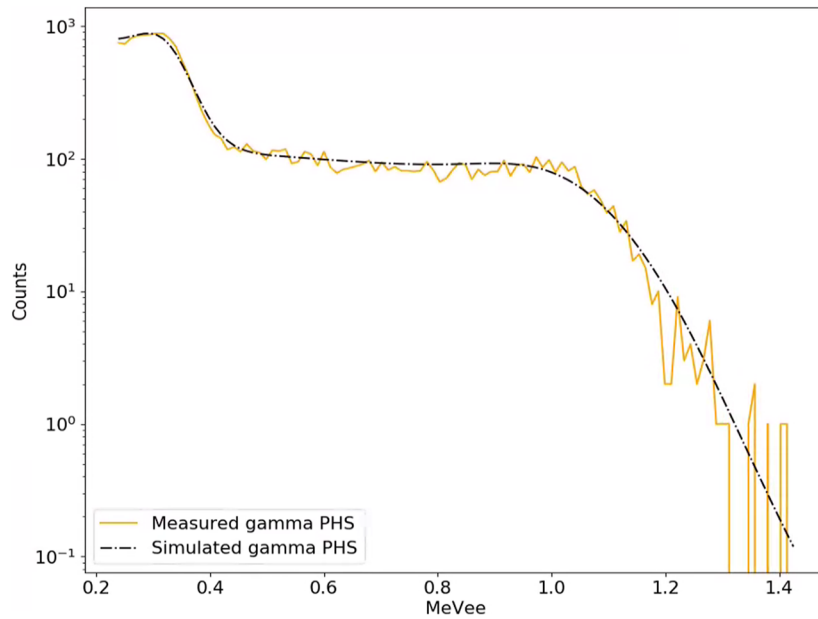


FIG. 7. Light yield calibration fit for JET shot 96 095 channel 6. The fitted parameters are $k = 18.8$, $m = 0.024$, $a = 0.0070$, $b = 0.032$, and $c = 19.8$.

be Poisson distributed, whereas for χ^2 it is assumed to be normal distributed. The resolution parameters are much correlated. The parameter a is usually close to 0, b varies roughly between 0.01 and 0.04, and c varies roughly between 20 and 200. The great

variation in c is because ^{22}Na spectrum does not provide information for higher energies. The resulting resolution parameters are then used for Gaussian broadening in all subsequent simulations with the detector system model. As a simplification this first fit is only

05 March 2024 13:50:23

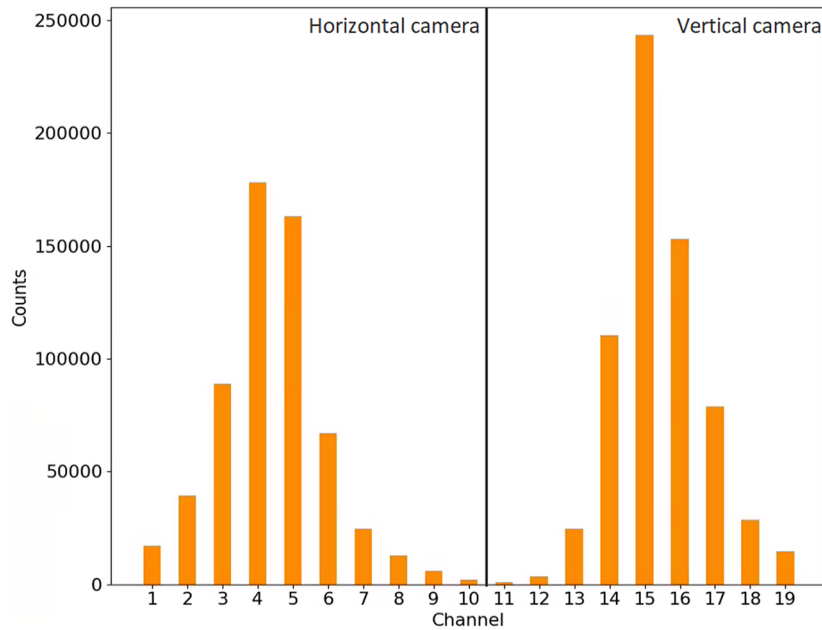


FIG. 8. Neutron counts in each channel of the neutron camera above a lower energy threshold of 0.5 MeVee. Data sourced from JET shot 92 306 in the time interval 47–49 s.

done for detector channel 14, though the resolution parameters are used for all channels. The light yield response is then simulated in the detector system model a second time, now for all channels and with Gaussian broadening included. The measured gamma PHS are fitted to the new simulated gamma PHS, which yields a set of calibration parameters k and m for each detector. An example of a light yield calibration fit is shown in Fig. 7. The calibration parameters are used to convert the measured neutron PHS into light yield using Eq. (1).

C. Measured neutron emission profile

Measurement data from the neutron camera channels can be arranged to describe a neutron emission profile. The measured PHS from Sec. III A are light yield calibrated according to Sec. III B for all channels. The neutron counts in each spectrum are then summed above an energy threshold of 0.5 MeV. An example of the resulting neutron counts for each channel is shown in Fig. 8.

IV. SIMULATING THE NEUTRONS

The neutron emission profile Δ is modeled based on the simplification that neutron emissivity is constant on the magnetic flux surfaces in the plasma. It is described as

$$\Delta = r_n(1 - \rho^2)^\alpha, \quad (4)$$

where r_n is the neutron emissivity scaling factor, ρ is the normalized minor radius, and α is the peaking parameter. The normalized minor radius is estimated using EFIT++/JEC2020.³³

The profile in Eq. (4) is used with the LINE2.1 model to calculate the simulated neutron rate of the direct component. Because LINE2.1 is an optical model the neutron rate must be corrected to take attenuation, transmission, and in-scatter into account. The attenuation due to material in the vacuum vessel is simulated using the JET model. The transmission and attenuation due to material close to the detectors is simulated using the detector system model. The in-scatter correction is made by simulating the neutron transport through the collimators and their light yield response in the detector, also using the detector system model. This is handled by the system response matrix detailed in Sec. IV B. Because the light yield response from the secondary protons is non-linear, we also require a non-linear light yield function as described in Sec. IV A.

A. Light yield function

The 19 detectors in the neutron camera have individual light yield characteristics. This is due to imperfections in the manufacturing process and different radiation histories. Although this requires individual treatment, this work uses a light yield function measured by Adams as a common basis.³⁴ The function was measured for NE213 scintillators similar to those used in the JET neutron camera and relates incident proton energy to light yield. The Adams light yield function spans over two energy intervals as

$$L = \begin{cases} x_1 + y_1 \cdot E_p + z_1 \cdot E_p^2 + w_1 \cdot E_p^3 & 0 < E_p \leq 1.85 \text{ MeV} \\ x_2 + y_2 \cdot E_p + z_2 \cdot E_p^2 + w_2 \cdot E_p^3 & 1.85 < E_p \leq 16.74 \text{ MeV,} \end{cases} \quad (5)$$

TABLE I. Coefficients used in Eq. (5).

x_1	0.0	x_2	-0.2012
y_1	0.165 9	y_2	0.2870
z_1	0.010 49	z_2	0.0378
w_1	0.017 28	w_2	-0.0011

where L is the light yield, E_p is the proton energy, and the coefficients $x_1, y_1, z_1, w_1, x_2, y_2, z_2,$ and w_2 are listed in Table I.

The light yield function is slightly different for each detector. We can describe this difference between detectors as the light yield L determined by Eq. (5), being modified by a stretch factor $a_{stretch_i}$ in channel i . The light yield L_{meas_i} measured by the scintillator then becomes

$$L_{meas_i} = L \cdot a_{stretch_i}. \quad (6)$$

In order to estimate the stretch factors, we use measurement data from pure thermal plasma conditions. This data is taken from time periods in which the plasma is only subjected to ohmic heating. Thermal measurement data for individual DD plasma shots do not contain a lot of neutrons, therefore data summed from 996 JET shots is used. The sum is a selection between JET shot 86 701–87 700. The neutron spectra from a thermal plasma is well represented by a Gaussian centered on 2.5 MeV.¹ The full width half maximum is described as

$$FWHM = \sqrt{T_i}(a_1 + T_i \cdot (a_2 + T_i \cdot (a_3 + T_i \cdot a_4))), \quad (7)$$

where T_i is the ion temperature and the coefficients $a_1, a_2, a_3,$ and a_4 are estimated by the Van Belle and Sadler FPS code³⁵ (see Table II). In the determination of the stretch factors, the ion temperature is assumed to be 4 keV.

The Gaussian is folded with the system response matrix to produce a simulated neutron PHS. This spectrum is fitted to the measured thermal neutron PHS by varying $a_{stretch_i}$ in Eq. (6) to minimize CSTAT. Repeating the procedure for all channels yields the stretch factors, and by extension, specific light yield functions for each channel.

For some channels, even the sum of 996 shots does not provide nearly enough statistics to perform a reliable fit. This is the case for channels 8, 9, 10, and 11. For these channels, we use a sum of three shots 96 094, 96 095, and 96 099, which use both ohmic and neutral beam injection heating. An additional stretch factor, $b_{stretch_i}$, is obtained for these four channels by fitting the measured PHS of channel 14 to 8, 9, 10, and 11, respectively. Using the known stretch

TABLE II. Coefficients used in Eq. (7).

T_i	a_1	a_2	a_3	a_4
4 keV	82.564	0.140 118	-4.0749×10^{-3}	1.0103×10^{-4}

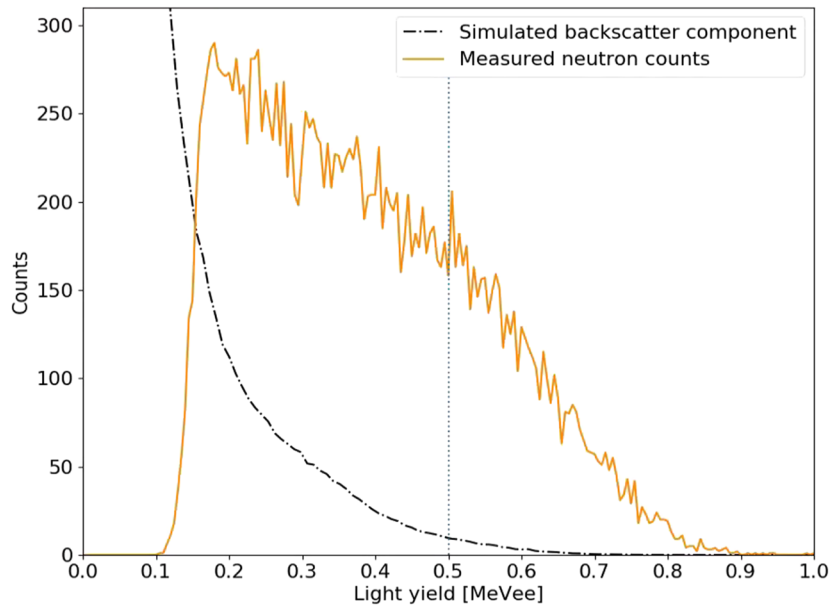


FIG. 9. Light yield calibrated pulse height spectrum of the selected neutron events in JET shot 96 095 channel 15 in the time interval 49.5–49.9 s. The backscatter component is simulated according to Sec. IV C. The lower energy threshold at 0.5 MeVee is marked with a dotted line. For the chosen energy threshold, backscatter neutrons make up a relatively small fraction of the total of neutrons above the threshold in channel 15.

factor, $a_{stretch_{14}}$, for channel 14, we can estimate the remaining stretch factors as

$$a_{stretch_i} = a_{stretch_{14}} \cdot b_{stretch_i}$$

where $a_{stretch_i}$ is the stretch factor for channel i .

However, this method is still not enough for channel 10, whose sightline results in a PHS containing mostly backscatter

events. For this reason, channel 10 is excluded from the rest of the analysis.

B. System response matrix

The system response matrix is used to calculate the detector light yield spectra for any neutron emission spectrum from the plasma, while accounting for in-scatter events. It is constructed

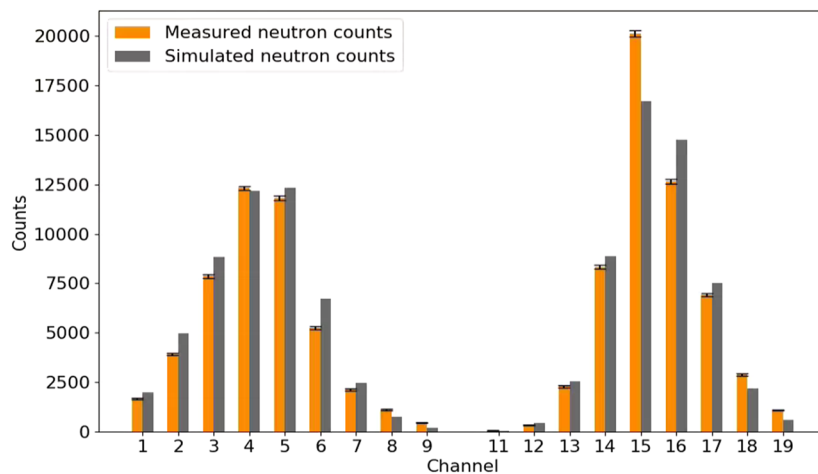


FIG. 10. Simulated neutron counts fitted to the measured neutron counts. Data sourced from JET shot 92 398 in the time interval 46.5–46.7 s. The measurement data are assumed to be Poisson distributed, which are used to estimate the uncertainties.

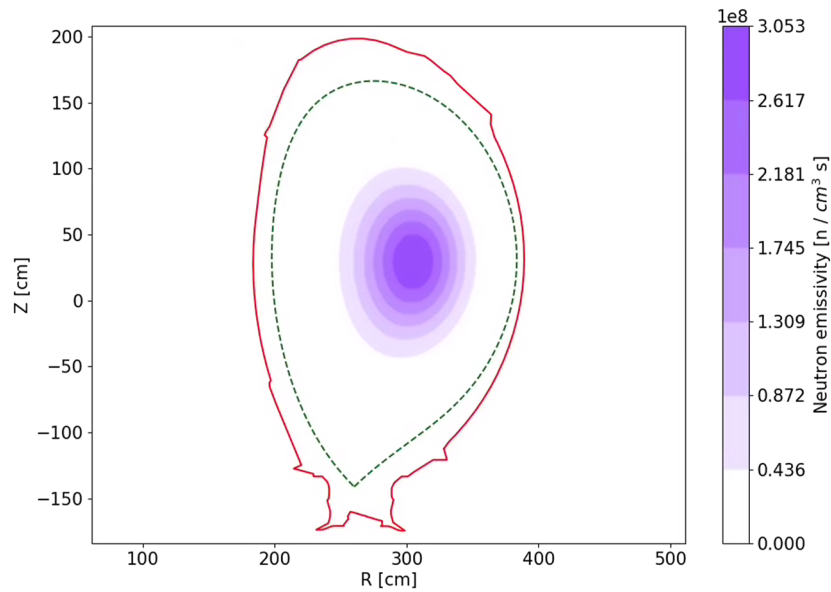


FIG. 11. Neutron emissivity profile corresponding to the fitted neutron response in Fig. 10. The dashed green line is the separatrix.

using two MCNP simulations with the detector system model. Simulation 1 treats all materials as perfect absorbers, imitating the optical LINE2.1 model. It calculates the total number of neutrons, N , that reach the detector. Simulation 2 allows neutron scattering and uses the light yield function described in Sec. IV A to calculate the scintillation light yield spectra, S , from neutrons in the detector. Both simulations use a monoenergetic neutron source placed at the collimator opening closest to the plasma, covering the whole opening.

To construct one row of the system response matrix, we calculate S/N , where each row corresponds to a monoenergetic neutron source. Because the two simulations use the same source, this ratio describes the increase in neutron rate, relative to the neutron rate calculated by LINE2.1, on the detector due to in-scatter and transmission. With repeated simulations for a range of monoenergetic neutron sources in 0.05 MeV steps, the system response matrix is created. For the direct component from a DD plasma, we expect neutrons close to 2.5 MeV. By summing that corresponding row in

05 March 2024 13:50:23

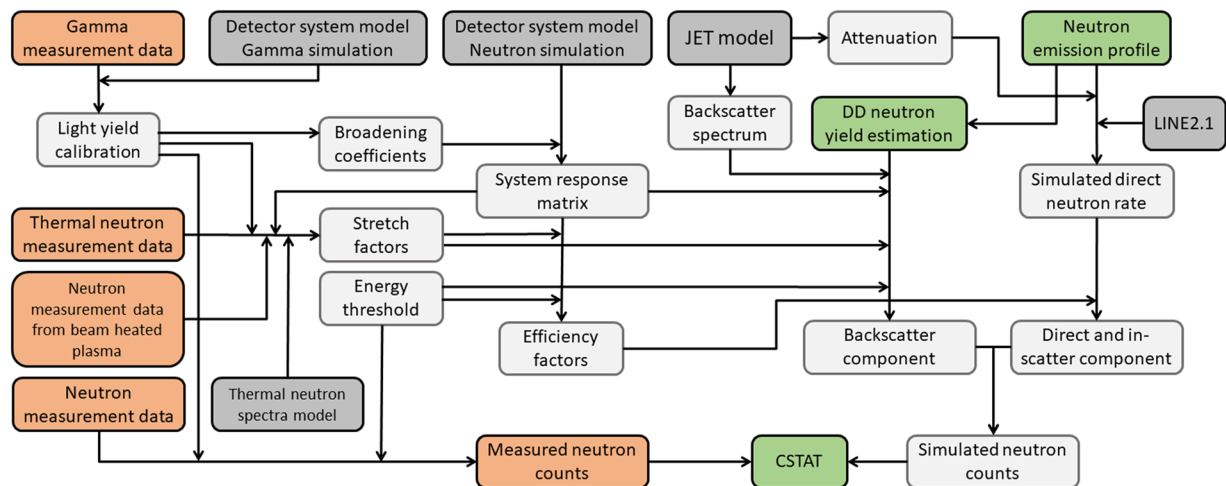


FIG. 12. Method overview for how CSTAT is calculated in the procedure. Measurement data are shown in orange boxes, models in dark gray, intermediate steps in white. The green boxes show steps related to our end product, the DD neutron light yield, which is chosen for the neutron emission profile that results in the smallest CSTAT. This overview underlines that the method is independent of other diagnostic systems except for the determination of the magnetic flux surfaces.

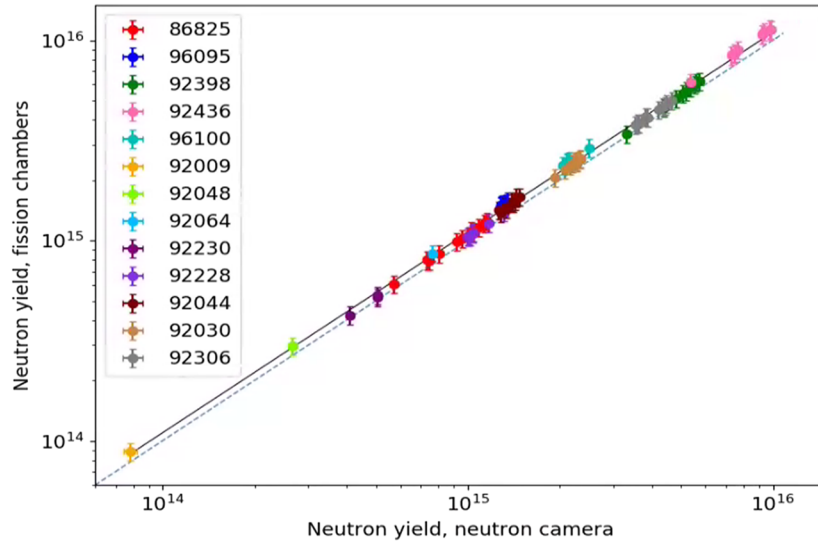


FIG. 13. Comparison between neutron yield estimates from the neutron camera and the fission chambers. The dashed line shows perfect agreement with a slope of 1. The solid line is fitted to all measurement points using orthogonal distance regression.

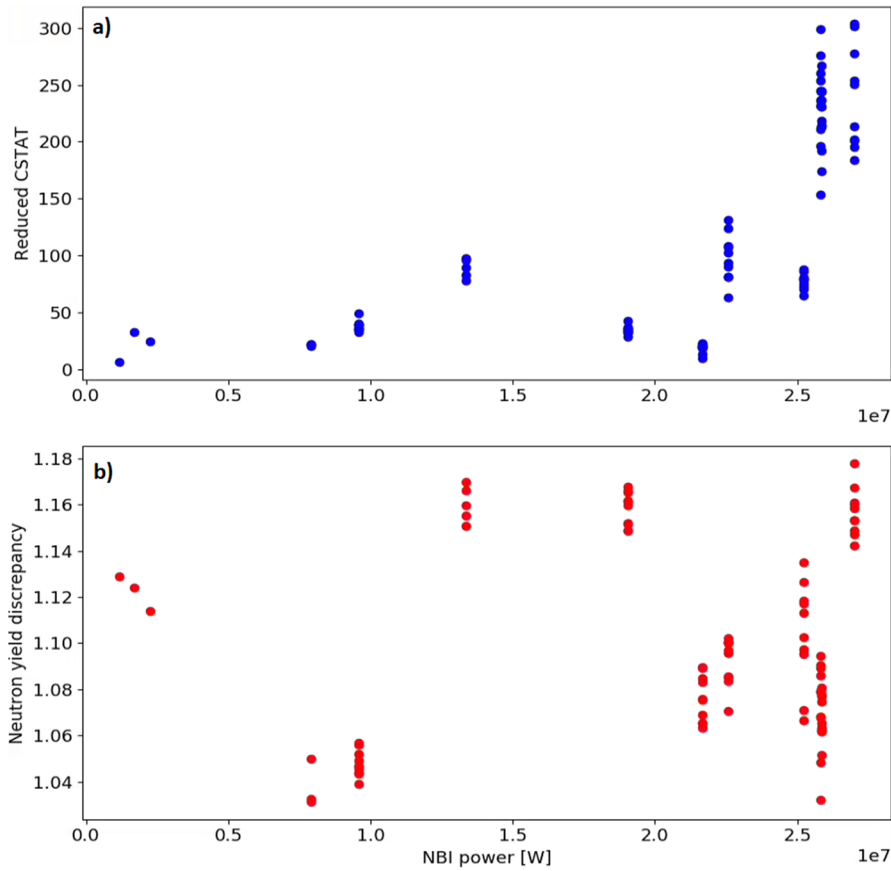


FIG. 14. The relationship between (b) NBI auxiliary heating power, and (a) CSTAT and neutron yield estimate discrepancy, respectively.

05 March 2024 13:50:23

the system response matrix above the energy threshold 0.5 MeVee, we obtain an efficiency factor. This must be done separately for each channel because of their individual light yield functions. The efficiency factor is then applied to the simulated neutron rate to estimate the direct component, including the in-scatter component, of neutron counts in each channel.

C. Backscatter

The JET model is used to simulate the neutron spectrum on the detectors due to neutrons scattering against the JET torus wall. This backscatter spectrum is in units of neutrons per the number of neutrons produced in the plasma. To obtain the intensity of the simulated backscatter component, the backscatter spectrum is scaled with the neutron yield estimated by the neutron emissivity profile (see Sec. IV D). The backscatter spectrum is then converted to a light yield spectrum by folding it with the system response matrix. The light yield of each channel is also adjusted with their respective stretch factors to account for the individual light yield functions. Summing the spectra above the same 0.5 MeVee threshold

yields the neutron counts due to the backscatter component in each channel.

The light yield calibrated measured PHS is shown for channel 15 in Fig. 9 together with the expected backscatter contribution. For this central channel, the energy threshold excludes the majority of backscatter neutrons. In contrast, some edge channels are completely dominated by the backscatter component.

D. Neutron yield estimation

The estimation of neutron counts in each channel is the sum of the simulated direct, in-scatter, and backscatter components. The direct and in-scatter components depend on the shape of the neutron emission profile and the backscatter component depends on the profile's corresponding neutron yield. A fit is performed by iterating over a range of profile peaking factors α [see Eq. (4)] to minimize CSTAT. In each iteration of the procedure, the following steps are taken:

1. The direct neutron rate is calculated with LINE2.1 together with the neutron emission profile, followed by an

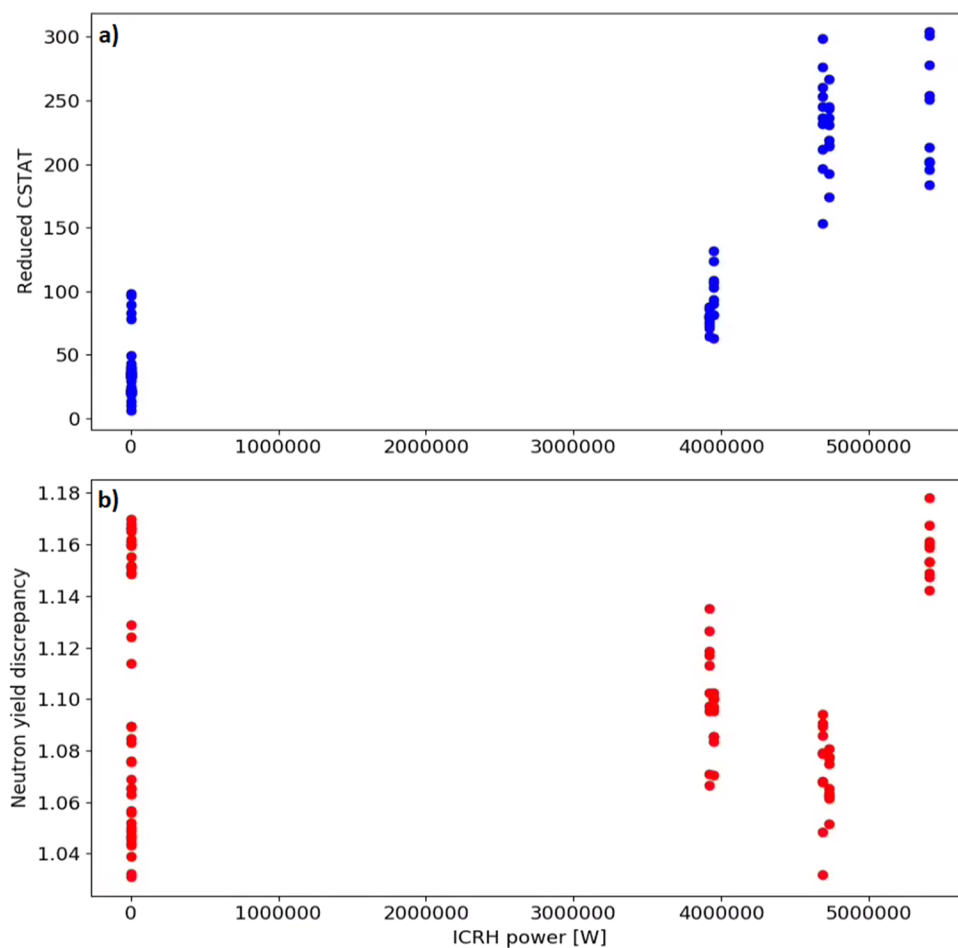


FIG. 15. The relationship between (b) ICRH auxiliary heating power, and (a) CSTAT and neutron yield estimate discrepancy, respectively.

estimation of direct and in-scatter counts using the efficiency factors.

2. The neutron yield is estimated by calculating the neutron emissivity in a rectangular grid for the current emissivity profile. Each grid square within the last closed flux surface is integrated toroidally and summed together to estimate a total neutron yield.
3. The backscatter component is estimated using the neutron yield, as described in Sec. IV C.
4. The simulated direct, in-scatter, and backscatter components are added together to form an estimation of simulated neutron counts in each channel. The scaling factor r_n is set such that the sum of all simulated neutron counts equals the sum of all measured counts across all channels. A CSTAT value is calculated when comparing the measured and simulated neutron counts in each channel.

An example of the fit in step 4 is seen in Fig. 10 and the corresponding neutron emissivity profile [see Eq. (4)] for the fitted α value in Fig. 11. For a fit that closely matches the measurement data, we estimate the total neutron yield for the corresponding α value and emissivity profile. An overview of the path from

models and measurement data to the final DD neutron yield estimate is seen in Fig. 12. Note that the method is independent of other diagnostic systems except for the determination of the magnetic flux surfaces.

V. RESULTS

The DD neutron yield has been estimated for a selection of 13 JET shots in a wide range of neutron yield intensities. Each estimate was compared to an estimation of the DD neutron yield from the JET fission chambers. The comparison is shown in Fig. 13 together with a dashed reference line representing a perfect agreement. In all cases, the neutron yield estimated by the fission chambers was larger than the neutron camera estimation. A line through the origin was fitted to all points in Fig. 13 using orthogonal distance regression to account for uncertainties in both estimates.³⁶ The slope of this line gave an average discrepancy of 9.6% larger neutron yield estimates from the fission chambers. The largest discrepancy among the selected shots is 17.8%, and the smallest is 3.1%. The uncertainties for the neutron camera yield estimates in Fig. 13 are the calculated statistical uncertainties based on the uncertainty of α

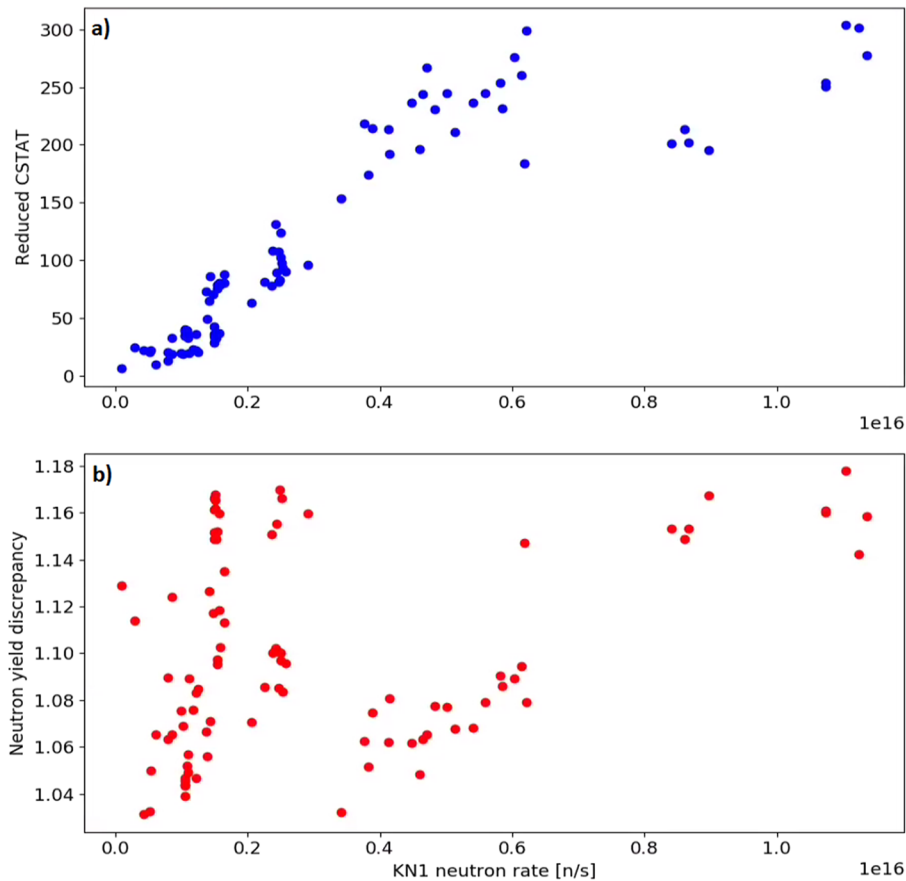


FIG. 16. The relationship between (b) neutron rate measured by the fission chamber, and (a) CSTAT and neutron yield estimate discrepancy, respectively.

[see Eq. (4)]. Systematic uncertainties in the MCNP model geometries will impact both calibrations and the response function, this is not yet included in the analysis. For the fission camera estimate, we assume an uncertainty of 10%.

The accuracy of the fit described in Sec. IV D is determined by the reduced CSTAT value. The discrepancy between the two DD neutron yield estimates is the ratio of the fission chamber estimate over the neutron camera estimate. These two quantities are plotted against the neutral beam injection power, the ion cyclotron resonance heating power, and the neutron rate measured by the fission chambers in Figs. 14–16.

The impact of attenuation, in-scatter, and transmission has been estimated for 2.45 MeV neutrons. According to the JET model, the attenuation through the portplate (see Fig. 1) is 8.4%. With the detector system model, the attenuation through the detector box wall and the plastic scintillator (see Fig. 2) is estimated to 42.6%. When including the effects of in-scatter and transmission in the detector system model, their contributions to the neutron rate above the 0.5 MeVee threshold are estimated to be 5.6% and 3.4% for in-scatter and transmission, respectively.

VI. DISCUSSION

This paper describes a first principle physics method for estimating the DD neutron yield using JET neutron camera measurements. The method uses modeling to simulate the transport, scatter, transmission, and attenuation of neutrons from the plasma. Most notably, this method accounts for the in-scatter component that, to our knowledge, has not been incorporated into previous analyses for the upgraded neutron camera geometry. For 2.45 MeV neutrons, the in-scatter and transmission makes up 5.6% and 3.4%, respectively, of the neutron rate above 0.5 MeVee. In-scatter and transmission might play a bigger role in the JET neutron camera than in other similar systems, since the diameters of the NE213 detectors are larger than their collimator apertures.

This method is the first to properly utilize the KN3N data acquisition system for the neutron camera. Since all pulse shapes are stored in the KN3 data acquisition system, it allows for a flexibility in the offline analysis. One such flexibility is in the separation between neutrons and gammas with pulse shape discrimination and an energy threshold.

This method for estimating the DD neutron yield is independent of other neutron measurements. It only depends on the JET neutron camera and the magnetic measurements used to calculate the normalized minor radius. The measurements are integrated along the camera sightlines. This makes the method insensitive to small changes in the normalized minor radius relative to the collimator openings, which are a few centimeters wide. The method also relies on JET neutron camera measurement data for a selection of JET shots for light yield calibration and for determining light yield functions.

The method produces a system response function that can convert any neutron spectrum from the plasma into a corresponding light yield spectrum. The DD neutron yield estimate uses a simplified parabolic model of the neutron emission profile, whose parameters are determined in a fit of the simulated neutron camera response to measured data. The simplicity of the neutron emission profile model is apparent from the large CSTAT values seen

in Figs. 14–16. While this is in part due to the high statistics of the measurement data, it is apparent that the model does not fully reflect the complexity of the plasma, as seen in Fig. 10. As noted, the assumption that the neutron emission is constant on the magnetic flux surfaces is a simplification. The fast ions in the plasma that generate neutrons will drift across flux surfaces. Neutron emission from trapped particles are especially not well described by the model. The neutron emissivity profile model used in this work has been extensively used in the past. Despite its notable shortcomings, it suffices to describe the neutron yield. This DD neutron yield estimate can be improved upon by considering more complex neutron emission profile models. Preliminary studies using a neutron emission profile modeled with TRANSP show promising results and will be used in future studies.

The method also has systematic uncertainties in the model geometry due to the lack of up to date JET neutron camera drawings, specifically ones showing the exact detector positions relative to the center of the plasma. The current analysis is based on older drawings. Despite this, the resulting DD neutron yield estimate is on average within a 10% agreement with the fission chamber DD neutron yield estimate.

The same methodology used in this paper can, and is planned to, also be applied to DT measurements to provide DT neutron yield estimates.

ACKNOWLEDGMENTS

This work was carried out within the framework of the EUROfusion Consortium, funded by the European Union via the Euratom Research and Training Program (Grant Agreement No. 101052200—EUROfusion). Views and opinions expressed are however those of the author(s) only and do not necessarily reflect those of the European Union or the European Commission. Neither the European Union nor the European Commission can be held responsible for them.

AUTHOR DECLARATIONS

Conflict of Interest

The authors have no conflicts to disclose.

Author Contributions

Linus Hägg: Conceptualization (equal); Data curation (lead); Formal analysis (lead); Investigation (lead); Methodology (lead); Project administration (lead); Software (lead); Validation (lead); Visualization (lead); Writing – original draft (lead); Writing – review & editing (lead). **Federico Binda:** Conceptualization (supporting). **Sean Conroy:** Conceptualization (equal); Formal analysis (supporting); Investigation (equal); Methodology (equal); Resources (equal); Software (equal); Supervision (equal); Validation (equal); Writing – review & editing (equal). **Göran Ericsson:** Conceptualization (equal); Funding acquisition (equal); Methodology (supporting); Project administration (equal); Supervision (equal); Writing – review & editing (equal). **Zamir Ghani:** Data curation (supporting); Resources (supporting); Writing – review & editing (supporting).

Luca Giacomelli: Data curation (supporting); Resources (supporting); Software (supporting); Writing – review & editing (supporting). **Daniele Marocco:** Data curation (supporting); Resources (supporting); Software (supporting); Writing – review & editing (supporting). **Alberto Milocco:** Data curation (supporting); Resources (supporting); Software (supporting); Writing – review & editing (supporting). **Marco Riva:** Data curation (supporting); Resources (supporting); Software (supporting); Writing – review & editing (supporting). **Erik Andersson Sundén:** Conceptualization (lead); Data curation (equal); Formal analysis (equal); Investigation (equal); Methodology (equal); Project administration (equal); Software (equal); Supervision (lead); Validation (equal); Visualization (equal); Writing – original draft (equal); Writing – review & editing (equal).

DATA AVAILABILITY

Raw data were generated at the JET large scale facility. Derived data supporting the findings of this study are available from the corresponding author upon reasonable request.

REFERENCES

- H. Brysk, “Fusion neutron energies and spectra,” *Plasma Phys.* **15**, 611–617 (1973).
- B. Wolle, “Tokamak plasma diagnostics based on measured neutron signals,” *Phys. Rep.* **312**, 1–86 (1999).
- A. S. Jacobsen, F. Binda, C. Cazzaniga, J. Eriksson, A. Hjalmarsson, M. Nocente, M. Salewski, G. Tardini, JET Contributors, and ASDEX Upgrade Team, “Velocity-space sensitivities of neutron emission spectrometers at the tokamaks JET and ASDEX Upgrade in deuterium plasmas,” *Rev. Sci. Instrum.* **88**, 073506 (2017).
- H. Järleblad, L. Stagner, M. Salewski, J. Eriksson, M. Nocente, J. Rasmussen, Z. Štancar, Ye. O. Kazakov, B. Simmendorf, and JET Contributors, “Fast-ion orbit sensitivity of neutron and gamma-ray diagnostics for one-step fusion reactions,” *Nucl. Fusion* **62**, 112005 (2022).
- C. Hellesen, M. Albergante, E. A. Sundén, L. Ballabio, S. Conroy, G. Ericsson, M. G. Johnsson, L. Giacomelli, G. Gorini, A. Hjalmarsson, I. Jenkins, J. Källne, E. Ronchi, H. Sjöstrand, M. Tardocchi, I. Voitsekhovitch, M. Weiszflog, and JET-EFDA Contributors, “Neutron spectroscopy measurements and modeling of neutral beam heating fast ion dynamics,” *Plasma Phys. Controlled Fusion* **52**, 085013 (2010).
- J. Eriksson, M. Nocente, F. Binda, C. Cazzaniga, S. Conroy, G. Ericsson, L. Giacomelli, G. Gorini, C. Hellesen, T. Hellsten *et al.*, “Dual sightline measurements of MeV range deuterons with neutron and gamma-ray spectroscopy at JET,” *Nucl. Fusion* **55**, 123026 (2015).
- M. Salewski, M. Nocente, A. S. Jacobsen, F. Binda, C. Cazzaniga, G. Ericsson, J. Eriksson, G. Gorini, C. Hellesen, A. Hjalmarsson, V. G. Kiptily, T. Koskela, S. B. Korsholm, T. Kurki-Suonio, F. Leipold, J. Madsen, D. Moseev, S. K. Nielsen, J. Rasmussen, M. Schneider, S. E. Sharapov, M. Stejner, M. Tardocchi, and JET Contributors, “MeV-range velocity-space tomography from gamma-ray and neutron emission spectrometry measurements at JET,” *Nucl. Fusion* **57**, 056001 (2017).
- O. N. Jarvis, “Neutron measurement techniques for tokamak plasmas,” *Plasma Phys. Controlled Fusion* **36**, 209 (1994).
- B. Esposito, F. B. Marcus, J. M. Adams, S. Conroy, O. N. Jarvis, M. J. Loughlin, G. Sadler, P. van Belle, and N. Watkins, “Ohmic ion temperature and thermal diffusivity profiles from the JET neutron emission profile monitor,” *Plasma Phys. Controlled Fusion* **35**, 1433–1440 (1993).
- C. Hellesen, J. Eriksson, F. Binda, S. Conroy, G. Ericsson, A. Hjalmarsson, M. Skiba, M. Weiszflog, and JET-EFDA Contributors, “Fuel ion ratio determination in NBI heated deuterium tritium fusion plasmas at JET using neutron emission spectrometry,” *Nucl. Fusion* **55**, 023005 (2015).
- J. Eriksson, G. Castegnetti, S. Conroy, G. Ericsson, L. Giacomelli, C. Hellesen, and JET-EFDA Contributors, “Deuterium density profile determination at JET using a neutron camera and a neutron spectrometer,” *Rev. Sci. Instrum.* **85**, 11E106 (2014).
- G. Ericsson, S. Conroy, M. Gat Johnson, E. Andersson Sundén, M. Cecconello, J. Eriksson, C. Hellesen, S. Sangaroon, M. Weiszflog, and JET EFDA Contributors, “Neutron spectroscopy as a fuel ion ratio diagnostic: Lessons from JET and prospects for ITER,” *Rev. Sci. Instrum.* **81**, 10D324 (2010).
- G. Bonheure, S. Popovichev, L. Bertalot, A. Murari, S. Conroy, J. Mlynar, I. Voitsekhovitch, and JET-EFDA Contributors, “Neutron profiles and fuel ratio n_T/n_D measurements in JET ELMy h-mode plasmas with tritium puff,” *Nucl. Fusion* **46**, 725–740 (2006).
- C. Hellesen, E. A. Sundén, S. Conroy, G. Ericsson, L. Giacomelli, A. Hjalmarsson, M. G. Johnsson, J. Källne, E. Ronchi, M. Weiszflog, L. Ballabio, G. Gorini, M. Tardocchi, I. Voitsekhovitch, and JET-EFDA Contributors, “Validating TRANSP simulations using neutron emission spectroscopy with dual sight lines,” *Rev. Sci. Instrum.* **79**, 10E510 (2008).
- C. Hellesen, E. Andersson Sundén, S. Conroy, G. Ericsson, J. Eriksson, M. Gat Johnson, M. Weiszflog, and JET-EFDA Contributors, “Neutron spectroscopy results of JET high-performance plasmas and extrapolations to DT performance,” *Rev. Sci. Instrum.* **81**, 10D337 (2010).
- F. Binda, G. Ericsson, J. Eriksson, C. Hellesen, S. Conroy, E. A. Sundén, and JET EFDA Contributors, “Forward fitting of experimental data from a NE213 neutron detector installed with the magnetic proton recoil upgraded spectrometer at JET,” *Rev. Sci. Instrum.* **85**, 11E123 (2014).
- J. M. Adams, O. N. Jarvis, G. J. Sadler, D. B. Syme, and N. Watkins, “The JET neutron emission profile monitor,” *Nucl. Instrum. Methods Phys. Res., Sect. A* **329**, 277–290 (1993).
- O. N. Jarvis, J. M. Adams, F. B. Marcus, and G. J. Sadler, “Neutron profile measurements in the Joint European Torus,” *Fusion Eng. Des.* **34–35**, 59–66 (1997).
- D. B. Syme, S. Popovichev, S. Conroy, I. Lengar, L. Snoj, and JET EFDA Contributors, “Fusion yield measurements on JET and their calibration,” *Nucl. Eng. Des.* **246**, 185–190 (2012).
- M. Rapisarda, “Calibration of the neutron profile monitor diagnostic at Joint European Torus (JET) by means of the Monte Carlo code for neutron- and photon-transport MCNP,” *Proc. SPIE* **2339**, 276–280 (1995).
- S. Popovichev, L. Bertalot, M. Adams, A. Alekseyev, M. Angelone, C. D. Challis, S. Conroy, N. Hawkes, J. Hobirk, V. Kiptily, A. Kashuck, A. Krasilnikov, P. U. Lamalle, A. Murari, M. Pillon, K. Stammers, D. Stork, and JET EFDA Contributors, “Performance of neutron measurements during trace tritium experiments on JET,” in *Proceedings of the 31st EPS Conference on Plasma Physics, London, UK* (IOP Publishing, 2004), Vol. 28G.
- M. Riva, B. Esposito, D. Marocco, F. Belli, B. Syme, and JET EFDA Contributors, “The new digital electronics for the JET Neutron Profile Monitor: Performances and first experimental results,” *Fusion Eng. Des.* **86**, 1191–1195 (2011).
- H. Sjöstrand, E. Andersson Sundén, L. Bertalot, S. Conroy, G. Ericsson, M. G. Johnson, L. Giacomelli, G. Gorini, C. Hellesen, A. Hjalmarsson, J. Källne, S. Popovichev, E. Ronchi, M. Weiszflog, M. Tardocchi, and JET EFDA Contributors, “Fusion power measurement using a combined neutron spectrometer-camera system at JET,” *Fusion Sci. Technol.* **57**, 162–175 (2017).
- D. Marocco, B. Esposito, M. Riva, and JET-EFDA Contributors, “Exploration of ion temperature profile measurements at JET using the upgraded neutron profile monitor,” *Rev. Sci. Instrum.* **83**, 10D314 (2012).
- A. Zimbal, M. Reginatto, H. Schuhmacher, L. Bertalot, B. Esposito, F. Poli, J. M. Adams, S. Popovichev, V. Kiptily, A. Murari, and Contributors to the EFDA-JET Work Program, “Compact NE213 neutron spectrometer with high energy resolution for fusion applications,” *Rev. Sci. Instrum.* **75**, 3553 (2004).
- Saint-Gobain Crystals, Solid Plastic Scintillators, available at <https://www.crystals.saint-gobain.com/radiation-detection-scintillators/plastic-scintillators> from November 22, 2022.
- The EUROfusion internal Figures Database, available at <https://figures.jetdata.eu> from May 31, 2022.
- F. Binda, G. Ericsson, S. Conroy, and E. Andersson Sundén, “Calculation of the profile-dependent neutron backscatter matrix for the JET neutron camera system,” *Fusion Eng. Des.* **123**, 865–868 (2017).

²⁹M. G. Johnson, S. Conroy, M. Cecconello, E. Andersson Sundén, G. Ericsson, M. Gherendi, C. Hellesen, H. Hjalmarsson, A. Murari, S. Popovichev, E. Ronchi, M. Weiszflog, V. L. Zoita *et al.*, “Modeling and TOFOR measurements of scattered neutrons at JET,” *Plasma Phys. Controlled Fusion* **52**, 085002 (2010).

³⁰G. F. Knoll, *Radiation Detection and Measurement* (John Wiley & Sons, Inc., 2000).

³¹MCNP[®] USER'S MANUAL Code Version 6.2, section 3.3.5.18.

³²W. Cash, “Parameter estimation in astronomy through application of the likelihood ratio,” *Astrophys. J.* **228**, 939–947 (1979).

³³L. C. Appel, G. T. A. Huysmans, L. L. Lao, P. J. McCarthy, D. G. Muir, E. R. Solano, J. Storrs, D. Taylor, and W. Zwingmann, “A unified approach to

equilibrium reconstruction,” in *2006 33rd EPS Conference on Plasma Physics, Rome* (European Physical Society, 2006), p. P2.184.

³⁴S. Conroy, private communication (2022).

³⁵P. Van Belle and G. Sadler, “The computation of fusion product spectra from high temperature plasmas,” Proceedings of the Course Workshop on Basic and Advanced Techniques for Fusion Plasmas, Varenna **3**, 767 (1986).

³⁶P. T. Boggs and J. E. Rogers, “Orthogonal distance regression,” in *Statistical Analysis of Measurement Error Models and Applications: Proceedings of the AMS-IMS-SIAM Joint Summer Research Conference Held June 10–16, 1989*, Contemporary Mathematics Vol. 112 (American Mathematical Society, 1990), p. 186.